

Passive particles driven by self-propelled particle: The wake effect

Kai-Xuan Zheng(郑凯选), Jing-Wen Wang(汪静文), Shi-Feng Wang(王世锋), and De-Ming Nie(聂德明)

Citation: Chin. Phys. B, 2024, 33 (**4**): 044501. DOI: 10.1088/1674-1056/ad1a8d
Journal homepage: http://cpb.iphy.ac.cn; http://iopscience.iop.org/cpb

What follows is a list of articles you may be interested in

Rolling velocity and relative motion of particle detector in local granular flow

Ran Li(李然), Bao-Lin Liu(刘宝林), Gang Zheng(郑刚), and Hui Yang(杨晖)
Chin. Phys. B, 2022, 31 (**11**): 114501. DOI: 10.1088/1674-1056/ac7dc0

Quasi-canonicalization for linear homogeneous nonholonomic systems

Yong Wang(王勇), Jin-Chao Cui(崔金超), Ju Chen(陈菊), Yong-Xin Guo(郭永新)
Chin. Phys. B, 2020, 29 (**6**): 064501. DOI: 10.1088/1674-1056/ab8627

Turbulence modulation model for gas-particle flow based on probability density function approach

Lu Wang(王路), Jiang-rong Xu(徐江荣)
Chin. Phys. B, 2017, 26 (**8**): 084702. DOI: 10.1088/1674-1056/26/8/084702

Particle transport behavior in air channel flow with multi-group Lagrangian tracking

Hao Lu(卢浩), Wen-Jun Zhao(赵文君), Hui-Qiang Zhang(张会强), Bing Wang(王兵), Xi-Lin Wang(王希麟)
Chin. Phys. B, 2017, 26 (**1**): 014702. DOI: 10.1088/1674-1056/26/1/014702

Biomechanical behaviors of dragonfly wing: relationship between configuration and deformation

Ren Huai-Hui(任淮辉), Wang Xi-Shu(王习术), Chen Ying-Long(陈应龙), and Li Xu-Dong(李旭东)
Chin. Phys. B, 2012, 21 (**3**): 034501. DOI: 10.1088/1674-1056/21/3/034501

Passive particles driven by self-propelled particle: The wake effect

Kai-Xuan Zheng(郑凯选)[1], Jing-Wen Wang(汪静文)[1], Shi-Feng Wang(王世锋)[2,†], and De-Ming Nie(聂德明)[1]

[1] *Institute of Fluid Mechanics, China Jiliang University, Hangzhou* 310018, *China*
[2] *Department of Mechanical Engineering, Hangzhou Vocational & Technical College, Hangzhou* 310018, *China*

(Received 16 October 2023; revised manuscript received 14 December 2023; accepted manuscript online 4 January 2024)

This work focuses on numerically studying hydrodynamic interaction between a passive particle and a self-propelled particle, termed a squirmer, by using a two-dimensional lattice Boltzmann method (LBM). It is found that the squirmer can capture a passive particle and propel it simultaneously, provided the passive particle is situated within the squirmer's wake. Our research shows that the critical capture distance, which determines whether the particle is captured, primarily depends on the intensity of the squirmer's dipolarity. The stronger dipolarity of squirmer results in an increased critical capture distance. Conversely, the Reynolds number is found to have minimal influence on this interaction. Interestingly, the passive particle, when driven by the squirmer's wake, contributes to a reduction in the squirmer's drag. This results in a mutual acceleration for both particles. Our findings can provide valuable perspectives for formulating the principles of reducing the drag of micro-swimmers and help to achieve the goal of using micro-swimmers to transport goods without physical tethers.

Keywords: lattice Boltzmann method (LBM), self-propelled particles, particle-laden flow

PACS: 45.50.–j, 47.55.Kf, 47.85.–g **DOI:** 10.1088/1674-1056/ad1a8d

1. Introduction

Numerous scenarios, including the translocation of gut pathobionts,[1] drug delivery via artificial micro-swimmers[2] and their cargo-towing functionality,[3] and the mobility and delivery capabilities of micro-swimmers are crucial factors in selecting and designing swimmers for drug transportation, cargo-towing, and particle diffusion and collective motion.[4–6] Just as paramecium and E. coli navigate fluidic environments, artificial micro-swimmers can reach specific locations in such environments.[7]

Jeanneret *et al.*[8] found that swimming microorganisms' activity directly affects surrounding objects, enhancing diffusion beyond Brownian motion. This affects the spatial distribution of non-motile planktonic species and particulate drifters. They thought that the heterogeneous dynamics probably depends on the generic features of swimming microorganisms with front-mounted flagella near-field. Dai *et al.*[9] presented an artificial micro-swimmer capable of sensing and orienting itself according to the illumination direction of an external light source. Hua *et al.*[10] achieved the passive particles transportation by chirality of active particles and special structure of microchannel. In terms of targeted drug and cargo delivery in medical applications, Alapan *et al.*[11] introduced a biohybrid micro-swimmer that transforms red blood cells from passive cargo carriers to active and guided ones. Moreover, Davies Wykes *et al.*[12] developed a method of concentrating and sorting swimmers based on different speeds, enabling the transportation of cargo to intended locations. Large self-propelled speed could enhance the ability of nematic particles to escape from captured state.[13] Utilizing a microcarrier-based drug delivery system appears to be a promising solution to address the challenges of precise drug delivery.[14,15]

The spherical squirmer model, first proposed by Lighthill in 1952[16] and later expanded by Blake in 1971,[17,18] has been frequently used to simulate the self-propulsion of swimmers like bacteria and volvox, which have dense arrays of cilia on their surface.[19–21] Given that squirmers can be modified to capture key characteristics of micro-swimmer flow fields, they are now used to study various biological and synthetic micro-swimmers, including Chlamydomonas reinhardtii, Volvox (pullers), and E. coli (pushers).[22–24] Recent studies have also focused on the hydrodynamic efficiency of a micro-swimmer, such as self-propulsion speed and drag efficiency, due to shape deformation or the combination of swimmers and cargos.[25–27] Felderhof[28] examined the swimming velocity and rate of dissipation of a linear chain comprised of two or three small spheres and a larger sphere. Their findings revealed that Stokes' law is not suitable for estimating swimming speed. A comprehensive calculation of swimming speed and rate of dissipation, taking into account hydrodynamic interactions as presented here, is necessary. The study shows that small-amplitude spherical squirmers maintain degeneracy at high wave numbers, but not at low ones. This complexity appears in parameter regimes beyond ciliate swimming, even at small amplitudes. Boundary element numerical methods are employed to investigate swimming with increased deformation amplitudes, specifically concerning power efficiency and swimming performance.[29] Ouyang *et al.*[30] assessed the influence of swimming Reynolds numbers and as-

[†]Corresponding author. E-mail: wsf@hzvtc.edu.cn

© 2024 Chinese Physical Society and IOP Publishing Ltd

sembly models on assembly locomotion (where the squirmer and cargo are fixed together). The pusher-cargo model swims faster than other models at a finite Reynolds number and proves to be more efficient, with larger relative distances resulting in smaller carrying hydrodynamic efficiency. In contrast, the puller-cargo model is more stable than the cargo-puller model, and a larger distance leads to more unstable swimming.[30] Nie *et al.*[31] and Ying *et al.*[32] studied the movements and interactions of circular squirmers under gravity in a two-dimensional (2D) channel with finite fluid inertia and five typical locomotive modes were obtained. They found that pullers with higher pressure regions on their lateral sides are more prone to breakdown and stability loss. Low-pressure regions cause pullers to attract each other, while pushers never make contact, maintaining a distance, which increases with separation increasing. Bonds between squirmers, particularly, enforce constant spatial proximity and enhance emergent correlations via micro-swimmer-specific flow fields. It is worth noting that the swimming efficiency of paired powerful pullers is some orders of magnitude lower than that of paired pushers.[33] However, most of existing studies focus on the bound squirmer–squirmer, squirmer–obstacle or squirmer–cargo system.[34] The interaction between the squirmer and a passive particle remains largely unexplored. We found that pullers (a type of squirmer that gains thrust from the front) can tow the passive particle and even propel it forward. This insight could provide the information about designing an unfixed cargo–carrier delivery system, in which the squirmer's inherent properties alone transport the cargo without any other physical connection. Interestingly, the passive particle can also reduce the swimming drag of the puller.

2. Methods and boundary conditions

2.1. Lattice Boltzmann method

In this study, the fluid is modeled by using the lattice Boltzmann method. The discrete lattice Boltzmann equation for a single-relaxation-time model is expressed as follows:[35]

$$\begin{aligned} & f_i(\boldsymbol{r}+\boldsymbol{e}_i\Delta t, t+\Delta t) - f_i(\boldsymbol{r},t) \\ = & -\frac{1}{\tau}\left[f_i(\boldsymbol{r},t) - f_i^{(\mathrm{eq})}(\boldsymbol{r},t)\right]. \end{aligned} \tag{1}$$

Here, τ denotes the relaxation time. A 2D lattice Boltzmann equation model with nine discrete velocities (D2Q9 model) is set on a square grid with a grid spacing Δx. The equilibrium distribution function in the direction of i is $f_i^{(\mathrm{eq})}$ and given by

$$f_i^{(\mathrm{eq})} = w_i\rho\left[1+\frac{\boldsymbol{e}_i\cdot\boldsymbol{u}}{c_\mathrm{s}^2}+\frac{(\boldsymbol{e}_i\cdot\boldsymbol{u})^2}{2c_\mathrm{s}^4}-\frac{\boldsymbol{u}^2}{2c_\mathrm{s}^2}\right], \tag{2}$$

where c_s is the speed of sound and given by $c_\mathrm{s}=c/\sqrt{3}$, w_i denotes the weight factor in the D2Q9 model, $w_0=4/9$, $w_{1-4}=1/9$, and $w_{5-8}=1/36$. The discrete velocities are expressed as follows:

$$\boldsymbol{e}_i = \begin{cases} (0,0), & i=0, \\ (\pm1,0)c, (0,\pm1)c, & i=1\text{–}4, \\ (\pm1,\pm1)c, & i=5\text{–}8. \end{cases} \tag{3}$$

Specifically, the lattice speed $c=\Delta x/\Delta t$. A grid spacing of $\Delta x=1$ and unit lattice time of $\Delta t=1$ are used in this study. The density of fluid ρ and velocity $\boldsymbol{u}$ are obtained as follows:

$$\rho=\sum_i f_i, \quad \rho\boldsymbol{u}=\sum_i f_i\boldsymbol{e}_i. \tag{4}$$

The fluid density ρ is set to 1, i.e., $\rho=1$. The dynamic viscosity is set to be $\mu=\rho\nu$, where ν denotes the kinematic viscosity.

Using the Chapman–Enskog expansion, the macroscopic mass equation and momentum equation in the low-Mach-number limit can be obtained as follows:

$$\frac{\partial\rho}{\partial t}+\nabla\cdot(\rho\boldsymbol{u})=0, \tag{5}$$

$$\frac{\partial(\rho\boldsymbol{u})}{\partial t}+\nabla\cdot(\rho\boldsymbol{u}\boldsymbol{u})=-\nabla p+\mu\nabla^2\boldsymbol{u}. \tag{6}$$

2.2. Squirmer model

The squirmer model, proposed by Blake,[17,18] employs oscillatory fluctuations (including radial direction and normal direction) on the boundary of a spherical or circular particle to emulate the motion of a micro-swimmer with a ciliary array. Consequently, a 2D squirmer with a radius a can self-propel away from a stationary fluid due to its minor surface axisymmetric deformation. We studied the kinematics of squirmer motion in a computational domain filled with a Newtonian fluid and under no-slip conditions. This model is commonly simplified and considers the tangential surface velocity $\boldsymbol{v}_\mathrm{s}$ as follows:

$$\boldsymbol{v}_\mathrm{s}=(B_1\sin\theta+B_2\sin\theta\cos\theta)\boldsymbol{e}_\theta. \tag{7}$$

Here, θ and $\boldsymbol{r}$ denote the polar angle and radial coordinate, respectively, and $\boldsymbol{e}_\theta$ and $\boldsymbol{e}_r$ represent the polar unit vector and position unit vector, respectively, which are shown in Fig. 1. Constant B_1 is related to the steady-state swimming velocity of the squirmer $U_\mathrm{s}=B_1/2$. The types of squirmers, i.e., pullers ($\beta>0$), pushers ($\beta<0$), and neutral squirmers ($\beta=0$), are determined according to $\beta=B_2/B_1$, where B_2 is parameter of dipolarity and determined by β.

The squirmer propels itself with a velocity ($U_\mathrm{s}=B_1/2$) because a tangential surface velocity field is controlled by the dipolarity β. The swimming Reynolds number Re_s is given as follows:

$$Re_\mathrm{s}=\frac{B_1 d}{2\nu}. \tag{8}$$

In this study, the density of the squirmer and passive particle is $\rho_s = 1.01$. The precision of the grid d is set to $32\Delta x$, i.e., $d = 32\Delta x$, and the squirmer is modeled as a circular cell body with a diameter d.

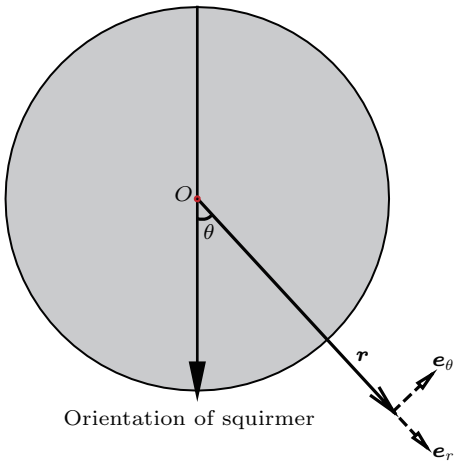


Fig. 1. Definition of polar angle θ and polar unit vectors $\boldsymbol{e}_\theta$.

2.3. Boundary conditions

In the lattice Boltzmann method, the moving boundary on the squirmer's surface requires special treatment to achieve a no-slip boundary condition. This study employs the improved bounce-back scheme proposed by Lallemand and Luo,[36] and the momentum transfer scheme proposed by Bouzidi *et al.*[37] Figure 2 provides a schematic of the scheme, in which the solid red squares, solid green circles, and white triangles represent solid, fluid, and boundary nodes, respectively. Following a collision, all solid and fluid nodes perform propagation actions; hence, the equilibrium distribution function from the solid nodes to the fluid nodes needs to be recalculated based on the precise locations of the boundary nodes.

To update f_5, nodes B, C, and D, which are located in the vicinity of node A are considered. The parameter $q = |AF|/|AB|$ is introduced to determine the location of the boundary node N. An interpolation scheme is used to recompute f_5 based on the surrounding nodes.

$$f_5(A) = \begin{cases} q(1+2q)f_7(B) + \left(1-4q^2\right)f_7(A) - q(1-2q)f_7(C) - 2w_7\rho_f \dfrac{e_7 \cdot u_N}{c_s^2}, & q < \dfrac{1}{2}, \\ \dfrac{1}{q(2q+1)}f_7(B) + \dfrac{2q-1}{q}f_5(C) - \dfrac{2q-1}{2q+1}f_5(D) - \dfrac{2w_7\rho_f}{q(2q+1)}\dfrac{e_7 \cdot u_N}{c_s^2}, & q \geq \dfrac{1}{2}. \end{cases} \tag{9}$$

In the above equation, u_N denotes the velocity of the moving surface at the boundary node N.

The bounce-back scheme proposed by Lallemand and Luo[36] uses a self-propelled velocity to update the velocity of boundary node N before interpolating Eq. (9)

$$\boldsymbol{u}_N = \boldsymbol{U} + \boldsymbol{\Omega} \times \boldsymbol{R} + \boldsymbol{v}_s. \tag{10}$$

Here, $\boldsymbol{U}$ and $\boldsymbol{\Omega}$ denote the translational velocity and angular velocity of the squirmer, respectively, and $\boldsymbol{R}$ represents the position vector from the center of mass of the squirmer to the boundary node N.

The force and torque exerted on the squirmer boundary node can be calculated by examining every flow–solid boundary link. It is also important to account for the additional force and torque generated by the transition between the fluid and solid nodes during the solid particle's motion; this is done by using the method proposed by Aidun *et al.*[38] The net force and torque can be determined by applying Newton's equation. Ultimately, the total force and torque are obtained by integrating the resulting force and torque as follows:

$$m\frac{\mathrm{d}^2\boldsymbol{x}}{\mathrm{d}t^2} = \boldsymbol{F}, \tag{11}$$

$$\frac{\mathrm{d}(J \cdot \boldsymbol{\Omega})}{\mathrm{d}t} = \boldsymbol{T}. \tag{12}$$

Here, m and $\boldsymbol{x}$ denote the mass of the squirmer and center of mass of the squirmer, respectively; $\boldsymbol{\Omega}$ and $\boldsymbol{J}$ represent angular velocity and momentum of inertia, respectively; and $\boldsymbol{F}$ and $\boldsymbol{T}$ refer to the force and torque, respectively.

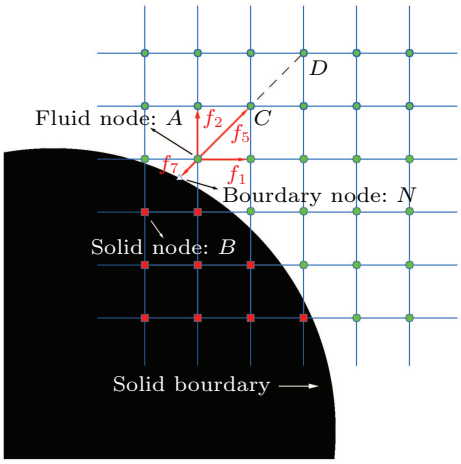


Fig. 2. Schematic diagram of bounce-back scheme in lattice Boltzmann method proposed by Lallemand and Luo, with solid red squares, green circles, and white triangles representing solid, fluid, and boundary nodes, respectively.

2.4. Collision model

The repulsive force model proposed by Glowinski *et al.*[39] is adopted to prevent the squirmer from penetrating the wall or any obstacles. A widely used collision strategy is implemented. Specifically, for handling interactions between the squirmer and the wall, as well as the squirmer and an obstacle, an approach is used that introduces an imaginary particle inside the wall.

$$F_{ij} = \begin{cases} 0, & d_{ij} > R_i + R_j + \Delta r, \\ \dfrac{c_{ij}}{\varepsilon}\left(\dfrac{d_{ij} - R_i - R_j - \rho}{\Delta r}\right)^2 \dfrac{\boldsymbol{G}_i\boldsymbol{G}_j}{d_{ij}}, & d_{ij} \le R_i + R_j + \Delta r, \end{cases} \tag{13}$$

Here, R_i and R_j denote the radii of particles i and j, respectively. Additionally, G_i and G_j denote the centers of mass of the particles, respectively. When the particle interacts with the wall, G_j is provided by the center of mass of the obstacle, as shown in Fig. 2. $d_{ij} = |G_iG_j|$, Δr indicates the region where the repulsive force begins to exist in the numerical simulation. Herein, $\Delta r = 2\Delta x$; c_{ij} indicates a force-scaling factor defined as the difference between the gravitational force and buoyant force of the micro-swimmer; ε denotes the stiffness coefficient and $\varepsilon = 10^{-3}$.

2.5. Computational conditions

In this study, we investigated the interaction between a puller and passive particle. As shown in Fig. 3, the puller is free to move, and its position corresponds to $\boldsymbol{G}_i = (x_i, y_i)$, whereas the passive particle is initialized at origin position $\boldsymbol{G}_j = (x_j, y_j)$. The puller was schematically represented in the computational domain with no-slip boundaries. The computational domain is $9d \times 12d$ in size. In Fig. 3, the solid blue circle indicates the position of a puller with a diameter d, whereas the solid black circle indicates the position of a passive particle with a diameter $d' = d/3$. The white arrow indicates the puller orientation and passive particle orientation. The upper boundary and lower boundary are at distance H_u and H_d from the center of the puller and obstacle, respectively. L_d denotes the distance from the left boundary to the center of the puller, S denotes the gap between the puller and obstacle. The computations were performed for $H_u = 8d$, $H_d = 4d$, $L_d = 4.5d$, and initial gap $S_0 = 0.5/1/1.5d'$.

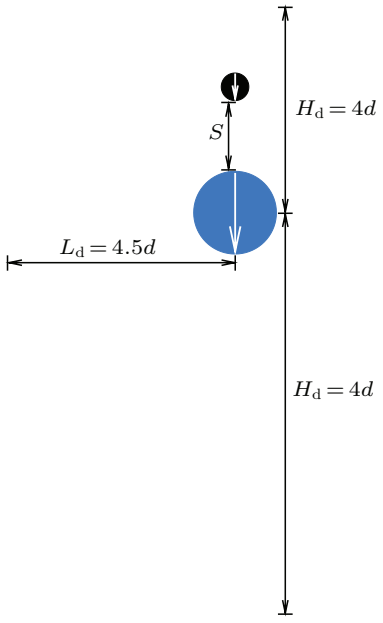


Fig. 3. Schematic diagram of present system and notations used in simulations. Unless otherwise stated, the computational domain is fixed as $9d \times 12d$ in size, corresponding to a computational domain of 864×1152 lattice units. We assume that the diameter of the puller is 96 lattice units. Initially, puller is placed at $(4.5d, 8d)$, and the passive particle is located at its initial position. In particular, passive particles are isotropic and arrows on the black circles only demonstrate deflection of the passive particles.

3. Validation

Validation was conducted to verify the computational code. As illustrated in Fig. 4, the Squirmer model was validated by comparing the squirmer's freely-swimming velocity with the theoretical solution $B_1/2$.[17] This is under the same conditions as in Section 2 but without the passive particle. In order to verify the grid accuracy ($d = 96\Delta x$), the squirmer was allowed to transition from static state to self-propelled state. Figure 4 demonstrates that the free-swimming velocity of the squirmer, under a squirmer diameter of $d = 96\Delta x$, satisfies the resolution ratio requirement.

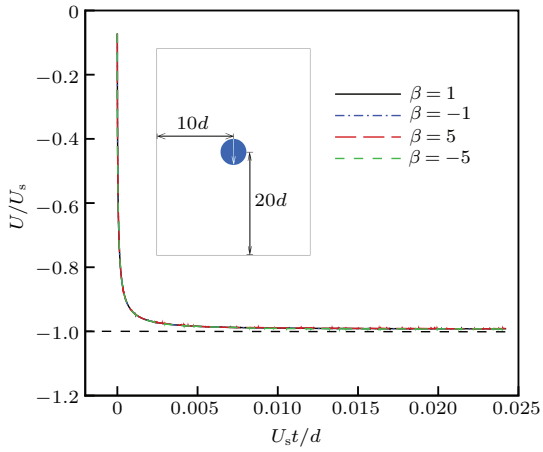


Fig. 4. Freely-swimming squirmer and time history of squirmer's velocity for different values of dipolarity β at $Re_s = 0.001$.

4. Results and discussion

4.1. Interaction between passive particle and puller

We investigate the process (attracting-subsequent-separating) between the puller and passive particle by using the settings described in Section 2. To identify the influences on the puller and passive particle, we change three parameters : the swimming Reynolds number Re_s, initial gap S_0, and dipolarity β of the puller. We select the value of Re_s in a range from 0.1 to 1, value of initial gap S_0 from 0.5 to $1.5d'$, and value of β from 1 to 5.

Two results are obtained. One is shown in Fig. 5(a), indicating that the passive particle is never captured by the puller, and the other is indicated in Fig. 5(b). It displays

the puller capturing passive particle and going through three stages: attracting-subsequent-separating. Hollow black circles and hollow blue circles represent as or future positions of passive particle and puller, respectively; solid black circles and solid blue circles denote current positions of passive particle and puller, respectively.

Figure 5 displays the pressure distributions and streamlines of the puller at different stages, which are crucial for determining whether the passive particle can be captured by the puller. This is due to the correlation between the strength of the puller's dipolarity and its low-pressure region. In Fig. 5(a), the puller with $\beta = 1$ pulls the passive particle forward for a certain distance and then drifts away. This occurs because the weak low-pressure area behind the puller is unable to capture the passive particle and swim alongside it. The puller with $\beta = 3$ captures and propels the passive particle during the capturing stage, but deviates and separates at the end as shown in Fig. 5(b). The passive particle is dropped after equilibrium has been disrupted, as it gets disturbed and deflected to one side. According to the study, the movement of passive particles near the puller is related to their streamline distribution. Consequently, the passive particles leave the side of the puller along the flow line.

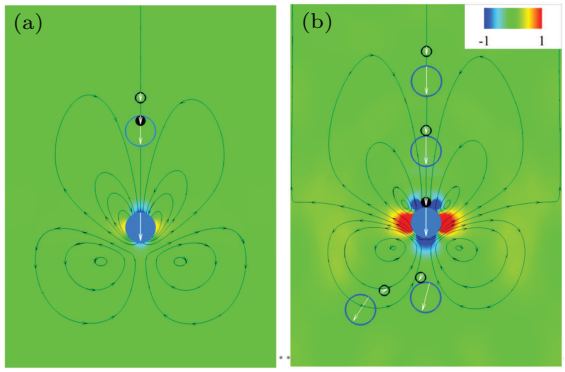


Fig. 5. Distributions of pressure (color contours) and streamline (solid black line with arrows) of the puller at different conditions with $S_0 = 1d'$, $Re_s = 0.5$, and $\beta = 1$ (a), with puller capturing no passive particle and moving alone, and 3 (b), with puller capturing passive particle and going through three stages: attracting-subsequent-separating. Hollow black circles and hollow blue circles represent as or future positions of passive particle and puller, respectively; solid black circles and solid blue circles denote current positions of passive particle and puller, respectively.

Furthermore, the velocities of the puller particle and passive particle exhibit significant differences at various stages. In Fig. 6(a), the puller propels the passive particle forward for a certain duration, but the puller's dipolarity is not strong enough to capture the passive particle, resulting in the passive particle slowing down and the puller keeping its free-swimming velocity.

Regarding the stage where passive particles are captured by the puller, the dynamic behaviors are entirely different. During the attraction phase, the passive particle accelerates and collides with the puller, achieving a maximum velocity significantly greater than U_s. Subsequently, the puller captures and carries the passive particle forward for a certain distance. Due to the drag-reducing effect of the passive particle on the puller, their swimming velocities are both faster than U_s. Ultimately, the puller and passive particle are separated from each other, and their velocities are no longer in synchronization.

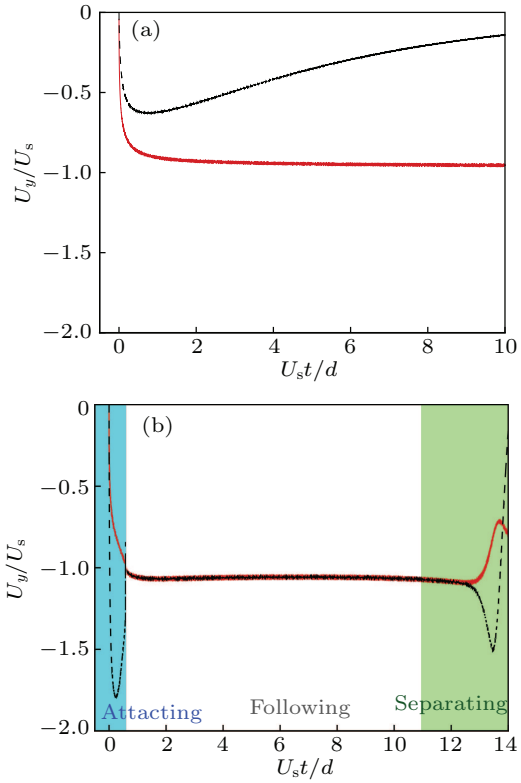


Fig. 6. Velocity of passive particle (black dashed line) and puller (red solid line) as a function of time with $S_0 = 0.5d'$, $Re_s = 0.1$, and $\beta = 1$ (a), with puller capturing no passive particle and moving alone, 5 (b), with puller capturing passive particle and going through three stages: attracting–subsequent–separating.

4.2. Critical capture distance

The analysis of state for the interaction between the puller and passive particle (Fig. 7(a)) shows that whether the puller can capture the passive particle (given β and S_0 are fixed, changes in Re_s do not affect the result) is unrelated to Re_s. However, β determines the critical capture distance (Fig. 7(b)): the stronger the puller's dipolarity (large β), the larger the critical capture distance is. This is attributed to the fact that the intensity of the pressure regions of the puller is determined by the strength of dipolarity β. The greater the dipolarity, the greater the strength and coverage of the puller's low-pressure area are, and hence the greater the critical distance is.

Figure 8 clearly shows that the puller with $\beta = 5$ has stronger low-pressure areas than that with $\beta = 1$, enabling the stronger puller ($\beta = 5$) to capture and draw the passive particle. For the same reason, the maximum velocity of the passive

particle during the attraction stage increases as β increases (Fig. 9(a)). The velocity during the subsequent stage slightly increases with β increasing, but this is due to the drag reduction of the puller when capturing a passive particle, which will be discussed later.

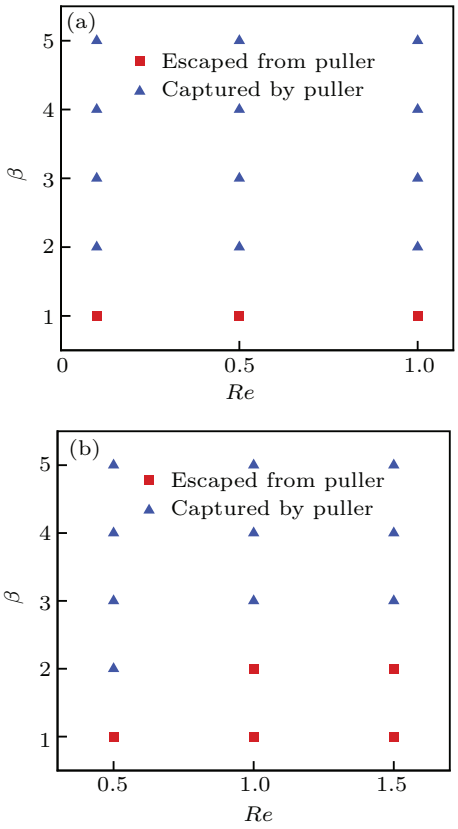


Fig. 7. (a) State diagram of interaction between puller and passive particle as a function of β and Re_s with $S_0 = 0.5d'$; (b) state diagram of the interaction between the puller and passive particle as a function of β and S_0 with $Re_s = 0.5$, with blue triangle indicating passive particle captured by puller and separated eventually, and red square denoting passive particle uncaptured by puller.

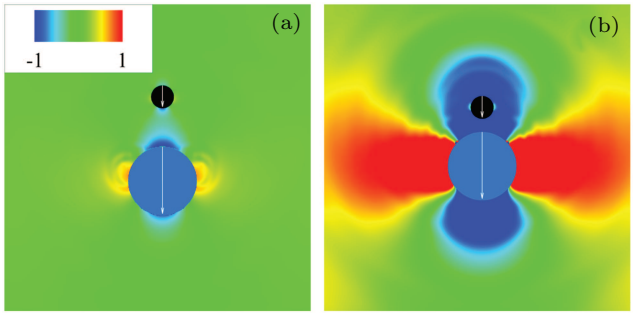


Fig. 8. Pressure distribution around squirmer in infinite fluid field at $Re_s = 0.5$ and $S_0 = d'$ for puller with $\beta = 1$ (a) and 5 (b).

Furthermore, we use three different sizes of passive particles to investigate the effect of passive particle size on critical capture distance, when the S_0 is fixed at $d/3$ so as to make sure that the gaps between the passive particle and the puller are the same. Unexpectedly, figure 9 shows that the size of the passive particle has no effect on whether the puller could capture the passive particle. The dipolarity of the puller seems to be the only determining variable.

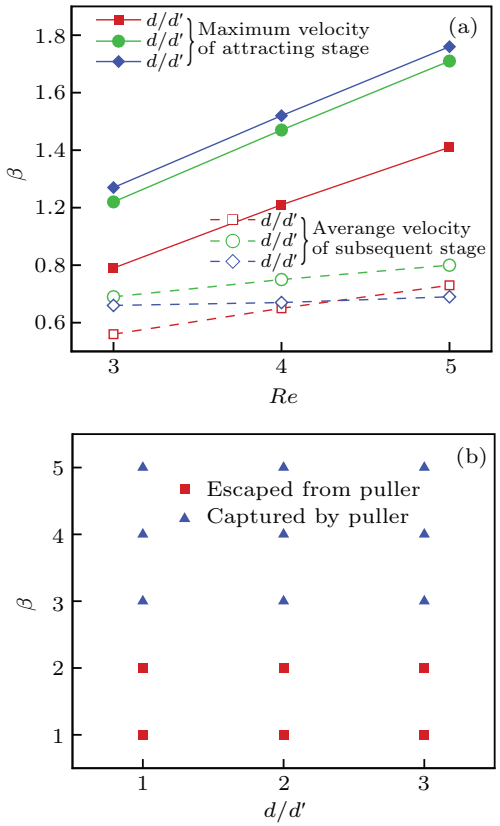


Fig. 9. (a) Velocity of passive particle at attracting stage and subsequent stage for different values of β and d/d' with $Re_s = 0.5$ and $S_0 = 0.5d'$. (b) State diagram of interaction between puller and passive particle as a function of β and d/d' with $Re_s = 0.5$ and $S_0 = d/3$, with S_0 fixed at $d/3$ to make sure that gaps between passive particle and puller are the same.

4.3. Drag reduction of puller

From Fig. 10, it is interesting to notice that the puller's swimming velocity is faster than its theoretical freely-swimming velocity when pulling a passive particle at a low swimming Reynolds number ($Re_s = 0.01,\ 0.1$). This occurs because the passive particle inhibits the expansion of the low-pressure area in the opposite direction of swimming, and concurrently fills the low-pressure region behind the puller, which is shown in Figs. 11(a) and 11(b). This effect results in reduced pressure resistance for the puller,

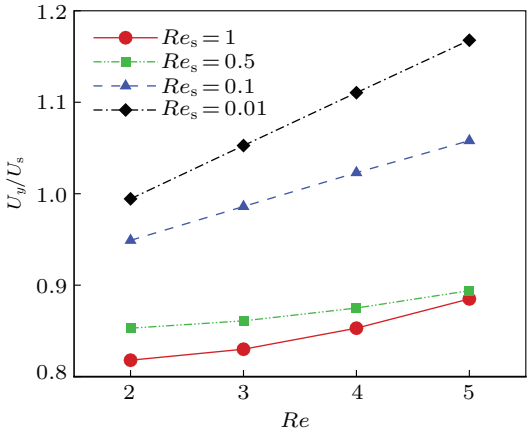


Fig. 10. Swimming velocity U_s for puller in subsequent stage (drawing the passive particle) at different values of β with $S_0 = 0.5d'$.

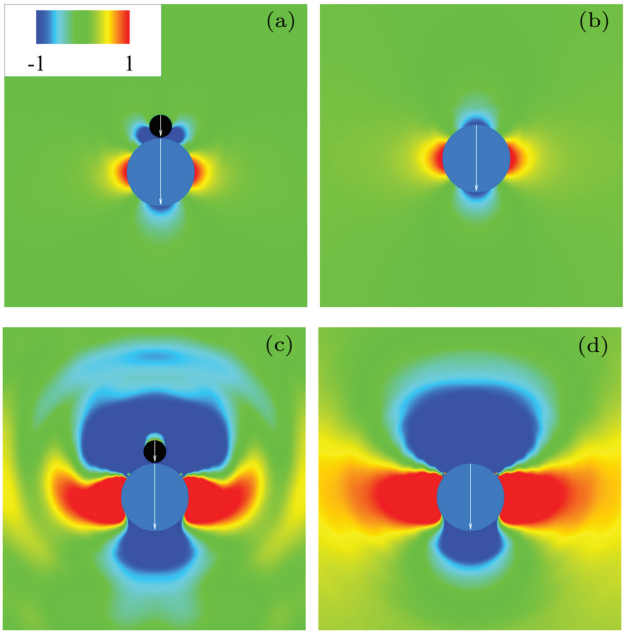


Fig. 11. Pressure distributions around squirmer in infinite fluid field with $\beta = 5$ for (a) the puller swimming with passive particle at $Re_s = 0.1$, (b) puller swimming without passive particle at $Re_s = 0.1$, (c) puller swimming with passive particle at $Re_s = 1$, and (d) puller swimming without passive particle at $Re_s = 1$.

enabling it to exceed its swimming speed. In particular, the low-pressure area behind the puller in this condition is primarily caused by the dipolarity of the puller.

However, at a larger swimming Reynolds number ($Re_s = 0.01, 0.1$), the puller swims slower than its theoretical freely-swimming speed when pulling a passive particle. As shown in Figs. 11(c) and 11(d), the low-pressure region becomes sufficiently strong to envelop the passive particle, thereby increasing the puller's pressure resistance. This occurs because the puller is loaded with the passive particle, which is too small to suppress and fill the low-pressure area behind the puller.

Furthermore, we investigate the effect of passive particle size on the swimming speed of the puller in the subsequent state. Figure 12 displays the pressure distributions of the puller with different sizes of passive particle, which shows that the larger passive particle fills more low-pressure areas. But the bigger the passive particle, the greater the mass that the puller needs to drive. This ultimately leads to a maximum speed of subsequent velocity of the puller at $d/d' = 2$ as shown in Fig. 9(a). It shows that there exists an optimal combination of d/d' and β, which maximizes the subsequent velocity of puller.

In addition, to investigate whether the capture mechanism functions in 3D case, we add a set of parameters under the same condition, specifically, $d/d' = 3$, $S_0 = d'$, $\beta = 5$, and $Re_s = 0.5$. As demonstrated in Fig. 13, the puller captures and propels the passive sphere, then moves ahead together. This is due to the same capture mechanism (low-pressure area behind the puller) of 2D simulations.

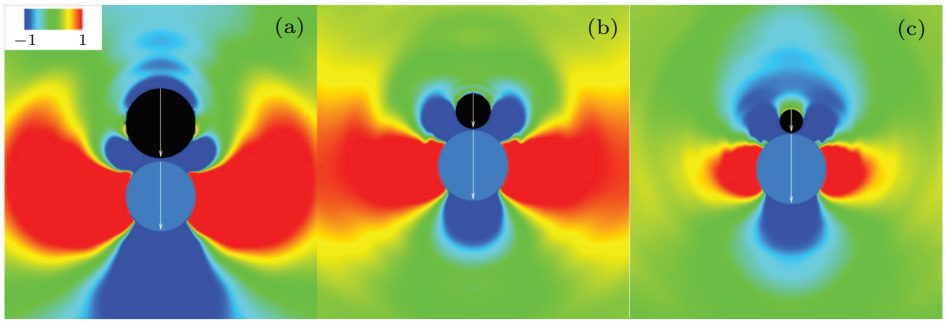


Fig. 12. Pressure distribution around squirmer in infinite fluid field with $\beta = 5$ for puller swimming with passive particle when $d/d' = 1$ (a), 2 (b), and 3 (c).

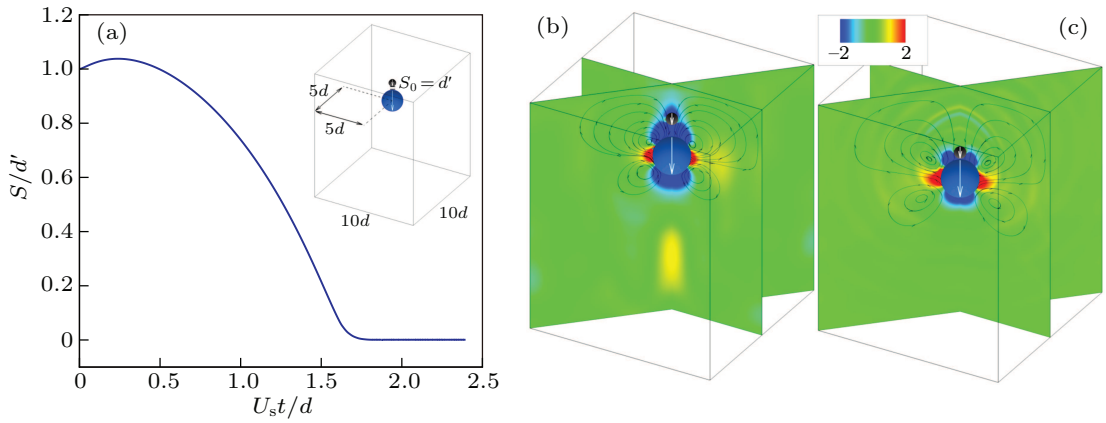


Fig. 13. Pressure distribution around squirmer in infinite fluid field with $\beta = 5$ in 3D simulation for (a) puller captured passive sphere with $d/d' = 3$, $S_0 = d'$, $\beta = 5$, and $Re_s = 0.5$; (b) puller and passive sphere in capture stage; and (c) puller and the passive sphere in subsequent stage.

5. Conclusions

In this work, the interaction and process (attracting-subsequent-separating) between a puller and passive particle is studied by using the lattice Boltzmann equation method. The effects of the puller's Reynolds number (Re_s), initial gap (S_0), and dipolarity (β) on the puller and passive particle throughout the attracting-subsequent-separating process are explored.

A puller with high dipolarity possesses a more potent low-pressure region behind it, which has the ability to capture and draw the passive particle forward. However, the passive particle is dropped by the puller after equilibrium has been broken due to the passive particle being disturbed and deflected to one side. This capture mechanism still functions in three-dimensional case, which is more relevant to real-world situation.

The β value determines the critical capture distance; a puller with stronger dipolarity (larger β) will have a greater critical capture distance. This is because a puller with stronger dipolarity maintains a more pronounced low-pressure region behind it, which is crucial for attracting and capture the passive particle. There is no effect of either Re_s or d/d' (the size of passive particle) on critical capture distance.

At the lower swimming Reynolds numbers ($Re_s = 0.01$, 0.1), the puller's swimming velocity is faster than the theoretical freely-swimming velocity when drawing a passive particle. This is attributed to the passive particle filling and restraining of the expansion of the low-pressure area behind the puller. In contrast, at larger swimming Reynolds numbers ($Re_s = 0.5$, 1), the puller's swimming velocity is slower than the theoretical freely-swimming velocity when drawing a passive particle. This slowdown is due to the increased strength of the low-pressure area, which becomes sufficient to enclose the passive particle and thus creates significant pressure resistance to the puller.

Acknowledgement

Project supported by the National Natural Science Foundation of China (Grant Nos. 12132015 and 11972336).

References

[1] Manfredo Vieira S, Hiltensperger M, Kumar V, Zegarra-Ruiz D, Dehner C, Khan N, Costa F R C, Tiniakou E, Greiling T, Ruff W, Barbieri A, Kriegel C, Mehta S S, Knight J R, Jain D, Goodman A L and Kriegel M A 2018 *Science* **359** 1156
[2] Schmidt C K, Medina-Sanchez M, Edmondson R J and Schmidt O G 2020 *Nat. Commun.* **11** 5618
[3] Gao W, Kagan D, Pak O S, Clawson C, Campuzano S, Chuluun-Erdene E, Shipton E, Fullerton E E, Zhang L, Lauga E and Wang J 2012 *Small* **8** 460
[4] Hu M, Ge X, Chen X, Mao W, Qian X and Yuan W E 2020 *Pharmaceutics* **12** 665
[5] Chen Y, Huang J, Meng F H, Li T C and Ai B Q 2021 *Chin. Phys. B* **30** 100510
[6] Wang Y, Shen Z, Xia Y, Feng G and Tian W 2020 *Chin. Phys. B* **29** 053103
[7] Park B W, Zhuang J, Yasa O and Sitti M 2017 *ACS Nano* **11** 8910
[8] Jeanneret R, Pushkin D O, Kantsler V and Polin M 2016 *Nat. Commun.* **7** 12518
[9] Dai B, Wang J, Xiong Z, Zhan X, Dai W, Li C C, Feng S P and Tang J 2016 *Nat. Nanotechnol.* **11** 1087
[10] Hua Y, He L and Zhang L 2017 *Chin. Phys. B* **26** 080702
[11] Alapan Y, Yasa O, Schauer O, Giltinan J, Tabak A F, Sourjik V and Sitti M 2018 *Sci. Robot.* **3** 17
[12] Davies Wykes M S, Zhong X, Tong J, Adachi T, Liu Y, Ristroph L, Ward M D, Shelley M J and Zhang J 2017 *Soft Matter* **13** 4681
[13] Zhu W J, Huang X Q and Ai B Q 2018 *Chin. Phys. B* **27** 080504
[14] Sharma M, Pandey C, Sharma N, Kamal M A, Sayeed U and Akhtar S 2018 *Anticancer Agents Med. Chem.* **18** 2078
[15] Klochkov S G, Neganova M E, Nikolenko V N, Chen K, Somasundaram S G, Kirkland C E and Aliev G 2021 *Semin. Cancer Biol.* **69** 190
[16] Lighthill M J 1952 *Commun. Pure Appl. Math.* **5** 109
[17] Blake J R 1971 *J. Fluid Mech.* **46** 199
[18] Blake J R 1971 *Math. Proc. Cambridge Philos. Soc.* **70** 303
[19] Pedley T J, Brumley D R and Goldstein R E 2015 *J. Fluid Mech.* **798** 165
[20] Pedley T J 2016 *Ima Journal of Applied Mathematics* **81** 488
[21] Kantsler V, Dunkel J, Polin M and Goldstein R E 2013 *Proc. Natl. Acad. Sci. USA* **110** 1187
[22] Theers M, Westphal E, Qi K, Winkler R G and Gompper G 2018 *Soft Matter* **14** 8590
[23] Uspal W E, Popescu M N, Dietrich S and Tasinkevych M 2015 *Soft Matter* **11** 434
[24] Holm C, Kremer K and Bolhuis P G 2009 *Advanced computer simulation approaches for soft matter sciences III* (Heidelberg: Springer Berlin) p. 237
[25] Daddi-Moussa-Ider A, Lisicki M and Mathijssen A J T M 2020 *Phys. Rev. Appl.* **14** 024071
[26] Ouyang Z, Lin Z, Yu Z, Lin J and Phan-Thien N 2022 *J. Fluid Mech.* **939** A32
[27] Ouyang Z and Lin J 2021 *Phys. Fluids* **33** 073302
[28] Felderhof B U 2014 *Phys. Rev. E* **90** 5
[29] Ishimoto K and Gaffney E A 2014 *Phys. Rev. E* **90** 012704
[30] Ouyang Z, Lin Z, Lin J, Yu Z and Phan-Thien N 2023 *J. Fluid Mech.* **959** A25
[31] Nie D, Ying Y, Guan G, Lin J and Ouyang Z 2023 *J. Fluid Mech.* **960** A31
[32] Ying Y, Jiang T, Nie D and Lin J 2022 *Phys. Fluids* **34** 1063
[33] Clopés J, Gompper G and Winkler R G 2020 *Soft Matter* 10676
[34] Zheng K, Wang J, Zhang P and Nie D 2023 *AIP Adv.* **13** 075011
[35] Qian Y, d'Humières D and Lallemand P 1992 *Europhys. Lett.* **17** 479
[36] Lallemand P and Luo L S 2003 *J. Comput. Phys.* **184** 406
[37] Bouzidi M, Firdaouss M and Lallemand P 2001 *Phys. Fluids* **13** 3452
[38] Aidun C K, Lu Y and Ding E J 1998 *J. Fluid Mech.* **373** 287
[39] Glowinski R, Pan T W, Hesla T I and Joseph D 1999 *Int. J. Multiphase Flow* **25** 755